Grain boundary density and electronic dual modulation of intermetallic Co2B by Fe doping toward efficient catalyst for oxygen evolution reaction

Xianshu Qiao [a],[1], Hongjun Kang [a],[b],[1], Yang Li [b], Kai Cui [b], Xin Jia [a], Xiaohong Wu [a],[b],[*], Wei Qin [a],[**]

[a] National Key Laboratory of Materials Behavior and Evaluation Technology in Space Environments, School of Materials Science and Engineering, Harbin Institute of Technology, Harbin, Heilongjiang 150001, PR China
[b] School of Chemistry and Chemical Engineering, Harbin Institute of Technology, Harbin, Heilongjiang 150001, PR China

ARTICLE INFO

ABSTRACT

Developing the high-performance intermetallic bi–metal boride OER catalysts with a high density of grain boundaries and appropriate electronic structure is still a challenge. Herein, we synthesized an intermetallic $(Fe_xCo_{1-x})_2B$ OER catalyst (GB-$(Fe_xCo_{1-x})_2B$) with controllable grain boundary densities by a facile ball-milling method. Benefiting from the modulation of both grain boundary density and electronic structure, the GB-$(Fe_{0.66}Co_{0.34})_2B$ supported on reduced graphene oxide shows a low OER overpotential of 221 mV at a current density of 10 mA cm^{-2} and Tafel slope of 38.2 mV dec^{-1}. The experimental and theoretical calculated methods demonstrate that the Fe introduction into the intermetallic Co2B catalyst can produce the higher grain boundary density and modulate the electronic structure, respectively. This work provides a promising insight in understanding the synergetic effects in bimetallic for GB-$(Fe_xCo_{1-x})_2B$ systems and supports a new strategy to explore other efficient catalysts with a high density of grain boundaries.

1. Introduction

Electrochemical water splitting to produce hydrogen, an attractive energy carrier, is a potential approach to solve the global energy crisis and the increasingly serious environmental issues [1]. However, the large-scale application of water electrolysis has represented a challenge for decades, owing to limitations such as the slow reaction kinetics and ineffective oxygen evolution reaction (OER) at the anode [2]. Therefore, the development of highly active and low-cost OER catalysts is a highly desirable goal to overcome these limitations. Noble metal-based catalysts such as IrO2 and RuO2 show excellent OER performance, but their widespread applications is hindered by their high cost, severe scarcity, and poor stability [3,4]. Hence, the development of earth-abundant OER catalysts with excellent performance and durability is a crucial long-term goal toward practical applications in water splitting.

Typically, an effective electro-catalyst for the oxygen evolution reaction must be a good electric conductor to enable the rapid extraction of generated electrons during intermediate steps [5]. Generally, metal alloy materials possess a better conductivity, especially for intermetallic metal–metalloid alloys, which are suitable OER materials owing to their metallic character, corrosion resistance, versatile compositions, as well as unique electronic and crystal structures [6]. Recently, as one of intermetallic transition metal–metalloid alloys, borides are expected to significantly boost the OER activity, as a new type of catalysts in alkaline electrolytes. For example, iron, nickel, and cobalt borides (Fe_xB, Ni_xB and Co_xB, respectively) are currently investigated [7–9]. Among these materials, cobalt borides exhibit outstanding activity. Moreover, Co2B has been reported to exhibit the best OER catalytic performance among various cobalt borides. For example, Masa et al. reported that amorphous Co2B exhibits superior OER activity to other Co_xB catalysts in alkaline solution [10]. Arya et al. elucidated the role of boron and stoichiometric ratio in the catalytic performance of Co–B materials using theoretical calculations [11]. Despite these major advances, the OER performance of Co2B is still limited, owing to the strong binding between metal atoms and intermediates, resulting from the slightly high electronegativity of Co (~1.88) [12]. A common approach to enhance the

---

OER activity involves tuning the electronic structure of the catalyst to adjust the binding strength between metal atoms and intermediates. Therefore, the partial substitution of Co with a relatively low electronegativity element such as Fe (~1.83), Mn (1.55), and Cr (1.66), etc could be used to control the overall electronegativity and electronic structure of the materials. Among these elements, the atomic radius of iron is equal to that of cobalt, which facilitates the replacement of cobalt by iron atoms. This could provide a moderate binding strength for OER intermediates and satisfy the Sabatier principle, endowing the obtained material with similar characteristics to effective noble metal catalysts.

In addition, a suitable catalyst must also possess a large quantity of active sites to ensure a high OER performance. The currently reported methods for increasing the number of catalytic active sites mainly include introducing conductive supporting structures and porous characteristic, fabricating 2D or 1D structures, and controlling the crystal morphology [13–16]. Although these methods can increase the exposed surface area of the catalysts to improve their catalytic active sites, the number of active sites is still insufficient for obtaining a high catalytic activity due to fundamental limitations on the lack of effective active sites on the inert surface [17]. Therefore, considering that the catalytic reactions are more likely to occur at the edge of the catalyst [18], constructing an electro-catalyst with a high grain boundaries density are proposed as an effective method to significantly increase the number of OER active sites. This is because the arrangement of atoms at the grain boundary is looser than that in the grain interior, and many defects such as vacancies, dislocations, and deformations are also present [19]. Unfortunately, intermetallic binary–metal borides with a high density of grain boundaries have rarely been reported. Thus, the development of a binary Fe–Co boride with a high density of grain boundaries is an urgent task to overcome the oxygen evolution limitations of present electro-catalysts.

In this work, we synthesized intermetallic $(Fe_xCo_{1-x})_2B$ OER electro-catalysts ($x = 0$, 0.33, 0.49, 0.66, 0.83 and 1) with controllable grain boundary densities by a facile ball-milling strategy (GB-$(Fe_xCo_{1-x})_2B$). Benefiting from the modulation of both grain boundary density and electronic structure, the GB-$(Fe_{0.66}Co_{0.34})_2B$ supported on reduced graphene oxide (GB-$(Fe_{0.66}Co_{0.34})_2B$/RGO) shows an enhanced OER activity. The optimized catalyst manifests a low OER overpotential of 221 mV at a current density of 10 mA cm^{-2} and Tafel slope of 38.2 mV dec^{-1}, both lower than the 275 mV and 84.6 mV dec^{-1} values of the pristine GB-Co$_2$B/RGO catalyst, respectively. In addition, using high-resolution transmission electron microscopy (HR-TEM) analysis and density functional theory (DFT) calculations, we demonstrate that the introduction of Fe in the intermetallic Co$_2$B catalyst could produce a higher density of grain boundaries and modulate the electronic structure. It is found that the higher the grain boundaries density could provide a higher number of active sites for the OER reaction due to the better electron transmission at the electrode/electrolyte interface. Moreover, the electronic control effect of the Fe-doped Co$_2$B, modifying the local electronic structure and redox properties at the grain boundaries, promoting the formation of OER intermediate species (MOO$^-$) during the OER process, and thus enhancing the OER activity of the GB-$(Fe_{0.66}Co_{0.34})_2B$ catalyst. These findings provide promising insights into the synergetic effects in bimetallic GB-$(Fe_xCo_{1-x})_2B$ systems and support a new strategy to explore other efficient catalysts with a high density of grain boundaries.

2. Experimental section

2.1. Materials

Cobalt powder (purity, >99.99%; diameter, ~500 nm), boron powder (purity, >99.99%; diameter, ~200 nm) and iron powder (purity, >99.99%; diameter, ~200 nm) were obtained from Aladdin Reagent Company, China. Potassium hydroxide (purity, >95%) was purchased from Tianjin Chemical Reagent Factory, China. All reagents were analytical grade and used without further purification.

2.2. Preparation of pristine GB-Co$_2$B and GB-$(Fe_xCo_{1-x})_2B$

The pristine GB-Co$_2$B and GB-$(Fe_xCo_{1-x})_2B$ catalysts were realized through a ball-milled method using a planetary ball mill (Fritsch Pulverisette 4). The feeding ratio of Fe/Co was controlled to obtain various GB-$(Fe_xCo_{1-x})_2B$ catalysts. Typically, 1.1 g Fe powder, 0.58 g Co powder, 0.32 g B powder, and 20 g zirconia wear-resistant grinding ball are added to agate jar with a zirconia material lining, and air in the grinding jar was removed by an Ar$_2$ (99.99%) inflation-deflation process to prevent the pollution caused by product oxidation. Rotational speeds and the reaction time were set to be 900 rpm and 10 h for all samples, respectively. The synthesis of pristine GB-Co$_2$B is similar to GB-$(Fe_xCo_{1-x})_2B$ except that the Fe powder was removed. In addition, the feed ratio of Co and Fe powder, as well as the name of the GB-$(Fe_xCo_{1-x})_2B$ obtained correspondingly are listed in Table S1.

2.3. Physical characterization

SEM measurements were performed using a Merlin Compact at an accelerating voltage of 20 kV (Carl Zeiss Company). SEM-EDS were carried out using a Teneo volume scope. TEM and HRTEM measurements were performed using a Tecnai G2 F30 transmission electron microscope with an accelerating voltage of 200 kV (FEI Company). Powder X-ray diffraction patterns were carried out using an Empyrean diffractometer (Panalytical company) assisted by monochromatic Cu-Kα radiation (λ = 1.54056 Å) within the 2θ range of 35–70°. X-ray photoelectron spectroscopy (XPS) measurements were performed on a ThermoFisher ESCALAB 250Xi spectrometer. XPSPEAK software (Ulvac-phi Company) was used for the XPS data processing. Raman spectra were acquired using a NANOFINDER spectrometer with 532 nm of the laser source wavelength. In situ Raman spectra were recorded on a Lab RENISHAW Raman Spectrometer with a laser excitation source of 532 nm for each spectrum, and the in situ Raman cell (Fig. S1) is produced by Shanghai Fan Yue Electronic Technology Co., Ltd (10 cm × 10 cm × 2.7 cm).

2.4. Electrochemical measurements

Electrochemical measurements of various catalysts were carried out using a CHI 660E workstation (Shanghai, China). A typical three-electrode system was used, with an Ag/AgCl as reference electrode, graphite rod as a counter electrode. Before the electrochemical test, the reference electrode was calibrated using Pt wire as the working electrode and counter electrode in high purity hydrogen saturated electrolyte solution, respectively. The GB-$(Fe_xCo_{1-x})_2B$ catalyst supported on reduced graphene oxide (RGO) was prepared by low-speed ball milling mixing reduced graphene oxide and as-catalyst with the weight ratios of 1:4 for 10 h in Ar gas atmosphere, then the obtained composite was added into 100 mL distilled water and ultra-sonicated for 60 min. The GB-$(Fe_xCo_{1-x})_2B$ supported on reduced graphene oxide catalyst was obtained by vacuum filtration of a well-scattered solution through a membrane filter. The GB-$(Fe_xCo_{1-x})_2B$ supported on reduced graphene oxide catalyst was loaded on carbon fiber paper with a size of 1 cm × 1 cm, which acted as the working electrodes for the electrochemical tests, and the mass loading on the RGO surface was about 0.7 mg·cm^{-2}. In addition, the GB-$(Fe_xCo_{1-x})_2B$ catalysts ink was also prepared by dispersing 5 mg catalysts in the mixed solution containing 350 μL ethanol, 130 μL water, 20 μL Nafion solution (5%, Sigma-Aldrich), and 5 μL loaded on glassy carbon electrodes (3 mm diameter) with a loading mass of approximately 0.7 mg cm^{-2}. LSV curves were recorded at 5 mV/s in O$_2$-saturated 1.0 M KOH. The polarization curves were *iR*-corrected and the potentials were converted in reference to the reversible hydrogen electrode (RHE, $E_{RHE} = E_{(Ag/AgCl)} + E_{0(Ag/AgCl)} + 0.059$ pH). Before measurement, Electrochemical impedance spectroscopy (EIS) data were collected at 1.531 V (versus the RHE) from a frequency range of 0.1 Hz to 100 kHz) and fitted by an equivalent circuit.

2.5. Computational detail

The GB-(Fe$_x$Co$_{1-x}$)$_2$B model with a 2 × 3 × 1 supercell was constructed to explore the synergetic role of Co and Fe in the binary metal boride catalyst. The density functional theory (DFT) was computed by Vienna ab initio Simulation Package (VASP). The projector augmented wave pseudopotential comprising the revised Perdew−Burke−Ernzerhof exchange-correlation functional was utilized to describe the interactions between core and electrons. An energy cutoff of 450 eV was used for the plane wave expansion of the electronic wave function. An 8 × 8 × 8, 8 × 8 × 4 Monkhorst Pack k-point setup were used for the slab geometry optimization of pristine GB-Co$_2$B and GB-(Fe$_x$Co$_{1-x}$)$_2$B, respectively. The force and energy convergence criteria were set to 0.02 eV Å^{-1} and 10^{-5} eV, respectively.

3. Results and discussion

3.1. Synthesis and structural characterization

The GB-Co$_2$B and GB-(Fe$_x$Co$_{1-x}$)$_2$B catalysts with different Fe/Co ratios were prepared by ball milling mixtures of iron powder, cobalt powder, and boron powder at the rotational speed of 900 rpm. The schematic of the synthetic procedure for the GB-(Fe$_x$Co$_{1-x}$)$_2$B is shown in Fig. 1a. Firstly, the SEM results (Fig. S2) detect that the as-prepared GB-Co$_2$B and GB-(Fe$_x$Co$_{1-x}$)$_2$B catalyst exhibit particle-like shapes with sizes of several hundreds of nanometers to 1 micrometer. Meanwhile, no significant changes in various GB-(Fe$_x$Co$_{1-x}$)$_2$B catalysts are observed for the particle size and surfaces roughness, which is also confirmed by particle size analysis results (Fig. 1b). The EDS element content analysis (Table S1) reveals that the Fe/Co atomic ratios of as-prepared samples are 0, 0.33, 0.49, 0.66, 0.83 and 1, respectively, which are denoted as GB-Co$_2$B, GB-(Fe$_{0.33}$Co$_{0.67}$)$_2$B, GB-(Fe$_{0.49}$Co$_{0.51}$)$_2$B, GB-(Fe$_{0.66}$Co$_{0.34}$)$_2$B, GB-(Fe$_{0.83}$Co$_{0.17}$)$_2$B and GB-Fe$_2$B.

XRD results plot in Fig. S3 show two broadened diffraction peaks
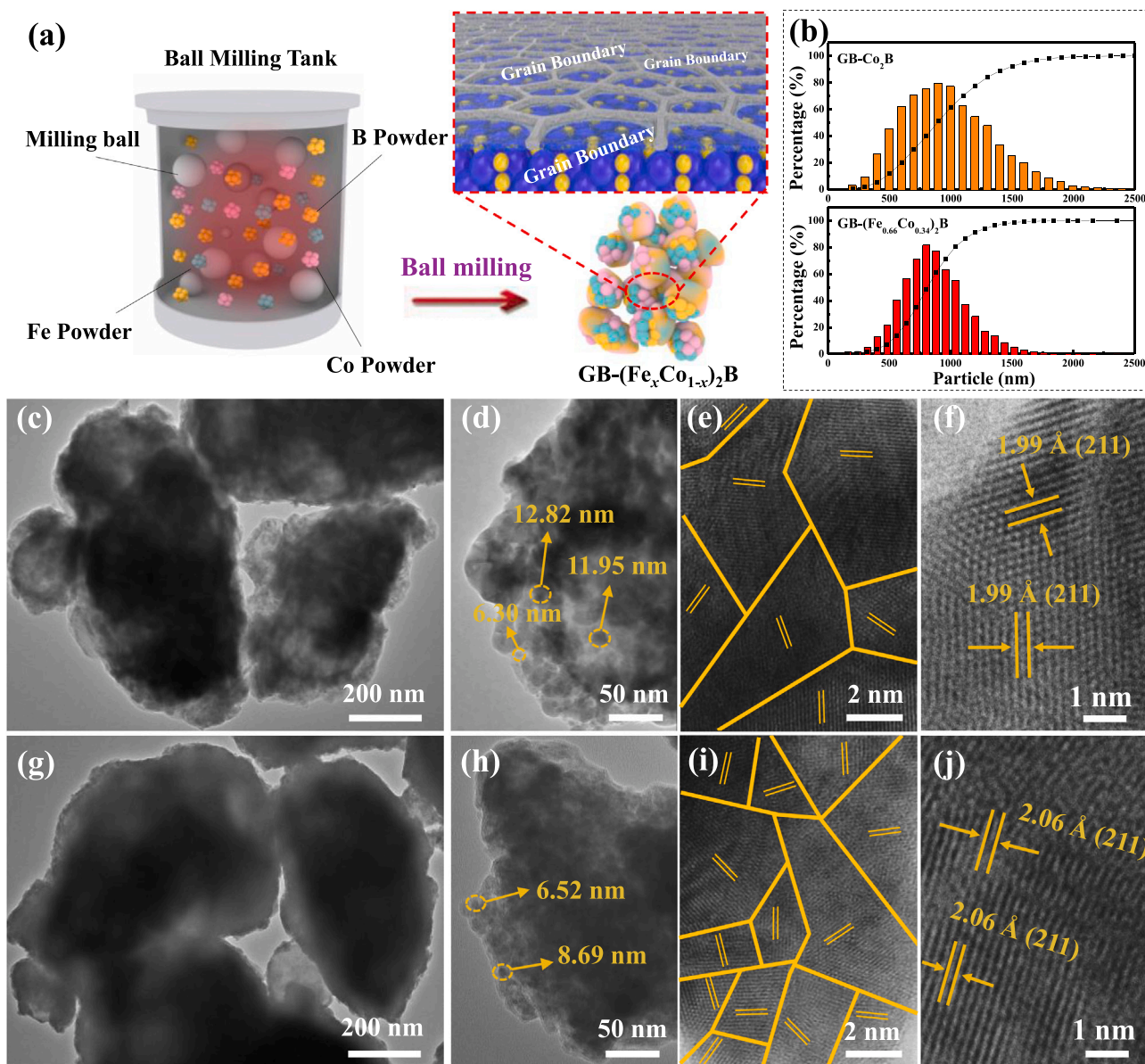

Fig. 1. (a) Schematic of the synthetic procedure for the GB-(Fe$_x$Co$_{1-x}$)$_2$B. (b) The particle size analysis for pristine GB-Co$_2$B and GB-(Fe$_{0.66}$Co$_{0.34}$)$_2$B. (c–f) TEM and HR-TEM images for pristine GB-Co$_2$B and GB-(Fe$_{0.66}$Co$_{0.34}$)$_2$B (g-j).

locate at 43.09° and 45.7° for the GB-Co$_2$B samples, which are attributed to the planes of (002) and (211) of the tetragonal Co$_2$B (JCPDS No. 25–0241), respectively. The position of (002) diffraction peak keeps unchanged with the increase of iron ratio, while the (211) diffraction peak shifts to smaller diffraction angles, indicating that the lattice is expanded along the (211) direction, which is mainly because of the atomic radius and electronegativity difference between cobalt atom and iron atom [20,21]. Based on XRD results, the lattice expansion rate is calculated, and the corresponded lattice expansion ratios normalized to pristine GB-Co$_2$B in these samples are 0.68% for GB-(Fe$_{0.33}$Co$_{0.67}$)$_2$B, 1.07% for GB-(Fe$_{0.49}$Co$_{0.51}$)$_2$B, 1.49% for GB-(Fe$_{0.66}$Co$_{0.34}$)$_2$B and 2.33% for GB-(Fe$_{0.83}$Co$_{0.17}$)$_2$B, respectively. The results show that the lattice expansion rate increases with the increase of iron cobalt ratio, indicating that the degree of lattice strain is increased. Furthermore, all as-synthesized samples appear the broadened XRD patterns peaks, which confirms that the grain size is as low as nanoscale and presents a short-range ordered structure. In fact, the small grains are unstable during the initial stage of ball milling, and these grains will accumulate into new big particles due to the reason that the smaller grains possess higher surface energy [22,23]. During the aggregation process, a large number of grain boundaries will be produced [24,25]. To this end, the grain size of as-prepared samples is also calculated based on the Scherrer equation, and the results are shown in Table S1. The pristine GB-Co$_2$B is 7.12 nm, which is much greater than that of GB-(Fe$_{0.33}$Co$_{0.67}$)$_2$B (4.85 nm), GB-(Fe$_{0.49}$Co$_{0.51}$)$_2$B (4.64 nm), GB-(Fe$_{0.66}$Co$_{0.34}$)$_2$B (4.60 nm), GB-(Fe$_{0.83}$Co$_{0.17}$)$_2$B (5.12 nm) and GB-Fe$_2$B (5.68 nm). Importantly, the higher density of the grain boundaries are generated during the aggregation process because of the smaller grain size [26]. Therefore, TEM, BET, Raman and XPS analysis for the pristine GB-Co$_2$B and GB-(Fe$_{0.66}$Co$_{0.34}$)$_2$B are used to explore the changes of the lattice strain and the density of grain boundaries.

As shown in Fig. 1c and g, TEM images show that the as-prepared GB-Co$_2$B and GB-(Fe$_{0.66}$Co$_{0.34}$)$_2$B catalyst exhibit particle-like shapes with sizes of around 1 micrometer. Meanwhile, there are many traces of the sub-grain aggregation and recombination for the particle-like sample, and it is observed that these individual nano-domains are interconnected through grain boundaries (Figs. 1d and 1h). HRTEM images (Fig. 1e and i) show generous lattice fringes with random orientation distribution for the as-prepared samples, and the GB-(Fe$_{0.66}$Co$_{0.34}$)$_2$B

possesses a more grain boundaries density compared to pristine GB-Co$_2$B, confirming the introduction of Fe in the intermetallic Co$_2$B catalyst could produce a higher density of grain boundaries [27–29]. The HRTEM image of GB-Co$_2$B nanoparticles (Fig. 1f) shows clear lattice fringes with spacing around 1.99 Å, which is attributed to the (211) plane of Co$_2$B. In contrast, the lattice space of the GB-(Fe$_{0.66}$Co$_{0.34}$)$_2$B (Fig. 1j) is enlarged to 2.06 Å, indicating that lattice is expanded along the (211) direction. Besides, the nitrogen adsorption-desorption isotherm curves (Fig. S4) show that the GB-(Fe$_{0.66}$Co$_{0.34}$)$_2$B also exhibits a higher specific surface area compared to pristine GB-Co$_2$B, further suggesting the GB-(Fe$_{0.66}$Co$_{0.34}$)$_2$B possesses a higher grain boundaries density. Raman spectra plot in Fig. 2a show that the two peaks at 214 cm^{-1} and 472 cm^{-1} for pristine GB-Co$_2$B are assigned to typical radial breathing modes of the stretching modes for the Co-B bond [30]. Compared with pristine GB-Co$_2$B, the Co-B bonds in GB-(Fe$_{0.66}$Co$_{0.34}$)$_2$B exhibit a red-shift toward the low wavenumber, which is mainly due to the phonon softening induced by tensile strain [31]. Further, the chemical surface properties and composition of the pristine GB-Co$_2$B and GB-(Fe$_{0.66}$Co$_{0.34}$)$_2$B are analyzed by XPS (Fig. 2b–f). The XPS survey spectrum plot in Fig. 2b confirms the presence of Co, Fe, B, and O elements, in which the O element derived from the surface oxidation upon exposure to the air. The high-resolution Co 2p spectrum (Fig. 2c) for pristine GB-Co$_2$B reveals the main peak at 778.6 eV is assigned to the Co species in Co$_2$B. On contrast, the peak in GB-(Fe$_{0.66}$Co$_{0.34}$)$_2$B has a slight shift toward the low bind energy compared to GB-Co$_2$B, suggesting that the introduction Fe in GB-Co$_2$B can turn the Co into electron-rich structure. The two peaks located at 781.05 and 782.85 eV for two samples can be ascribed to the CoO and Co(OH)$_2$ due to air exposure, respectively [32]. The B 1s spectrum (Fig. 2d) shows that the peak at around 192.2 eV corresponds to the high-valence state of B, such as boron-oxo species [10]. In addition, Fe 2p spectrum (Fig. 2e) shows that the GB-(Fe$_{0.66}$Co$_{0.34}$)$_2$B exhibits a binding energy at 706.9 eV, which is attributed to the formation of Fe–B bonds in GB-(Fe$_{0.66}$Co$_{0.34}$)$_2$B. The peaks located at 713.15 eV and 711.15 eV are assigned to FeO and Fe(OH)$_x$, respectively. Fig. 2f displays that the O species at 532.8 eV is typical for adsorbed O–O bonds. Compared with pristine GB-Co$_2$B, an obvious increase in the intensity of adsorbed O–O (free oxygen) on GB-(Fe$_{0.66}$Co$_{0.34}$)$_2$B, which suggests the enhanced binding strength of GB-(Fe$_{0.66}$Co$_{0.34}$)$_2$B surface to oxygenated
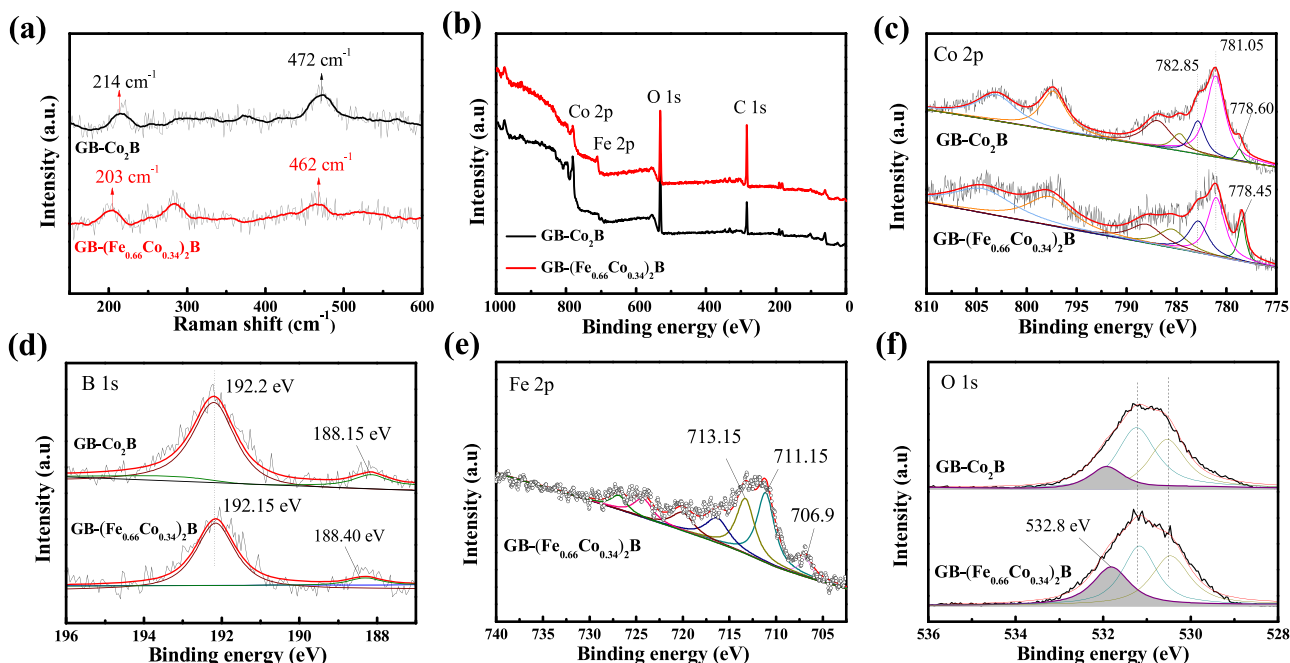

Fig. 2. (a) Raman spectra. (b-f) XPS spectra of GB-Co$_2$B and GB-(Fe$_{0.66}$Co$_{0.34}$)$_2$B. (b) XPS survey spectra. (c) Co 2p. (d) B 1 s (e) Fe 2p. (f) O 1 s.

intermediates [33]. Above results indicate that the introduction of Fe in Co_2B not only can generate the lattice strain without significantly altering their crystal structure but result in a higher grain boundary density.

3.2. OER activity of GB-Co_2B and GB-$(Fe_xCo_{1-x})_2B$

Since the OER catalytic active sites are only located in the redox-active near-surface region of ~3rd atomic layer of the catalysts and the exposed surface area of the catalyst strongly influences its catalytic activity [34]. Thus, the GB-$(Fe_xCo_{1-x})_2B$ catalyst supported on reduced graphene oxide catalyst (GB-$(Fe_xCo_{1-x})_2B$/RGO) is constructed (Fig. 3a). LSV curves show that the GB-$(Fe_{0.66}Co_{0.34})_2B$/RGO exhibits the highest OER performance among all as-prepared catalysts with the lowest overpotential of only 221 mV at a current density of 10 mA cm^{-2}(Fig. 3b), which is significantly better than those of pristine GB-Co_2B and other GB-$(Fe_xCo_{1-x})_2B$/RGO samples. Remarkably, the overpotentials of GB-$(Fe_{0.66}Co_{0.34})_2B$/RGO outperforms most newly reported nonprecious Co or Fe based systems catalysts [35–43] (Fig. 3c). Tafel slope of GB-$(Fe_xCo_{1-x})_2B$/RGO catalysts were also obtained from polarization curves to evaluate the OER reaction kinetics property. Fig. 3d shows that the GB-$(Fe_{0.66}Co_{0.34})_2B$/RGO exhibits a small Tafel slope of 38.2 mV dec^{-1}, which is much smaller than those of GB-Co_2B/RGO (84.6 mV dec^{-1}), GB-$(Fe_{0.49}Co_{0.51})_2B$/RGO (56.6 mV dec^{-1}), GB-$(Fe_{0.33}Co_{0.67})_2B$/RGO (78.4 mV dec^{-1}), GB-$(Fe_{0.83}Co_{0.17})_2B$/RGO (84.2 mV dec^{-1}) and

GB-Fe_2B/RGO (89.5 mV dec^{-1}). To more intuitively demonstrate the dynamics changes, the OER reaction activation energy (*Ea*) has been calculated from the slope of the Arrhenius plot (Fig. 3e) [44]. In comparison, the GB-$(Fe_{0.66}Co_{0.34})_2B$/RGO exhibits a lower *Ea* value of 10.68 kJ·mol^{-1} than GB-Co_2B/RGO, indicating that the introduction of Fe in Co_2B can effectively decrease the OER reaction energy barrier. Additionally, the GB-$(Fe_{0.66}Co_{0.34})_2B$/RGO catalyst demonstrates a 97.6% Faradaic efficiency for OER (Fig. 3f), and the measured data is conformed to the theoretical quantity of O_2. It is worth mentioning that the current density of GB-$(Fe_{0.66}Co_{0.34})_2B$/RGO at 1.46 V (vs. RHE) has no obvious decrease for 100 h (Fig. 3g), indicating that the GB-$(Fe_{0.66}Co_{0.34})_2B$/RGO also processes outstanding long-term stability. Besides, OER catalytic activity for various pure GB-$(Fe_xCo_{1-x})_2B$ is also determined using a loading on glassy carbon electrode method (Figs. S5–S7). The OER performance for GB-$(Fe_xCo_{1-x})_2B$ shows similar trends with GB-$(Fe_xCo_{1-x})_2B$/RGO, which further indicates that the introduction Fe in Co_2B can effectively promote the OER performance.

3.3. Mechanism of OER activity enhancement

As mentioned above, Fe doping has a significant impact on the OER activity of the Co_2B catalyst; hence, we have examined the mechanism behind the enhanced of activity of bimetallic GB-$(Fe_xCo_{1-x})_2B$ catalysts. First, we estimate the electrochemical double-layer capacitance (C_{dl}) to determine the real surface area of the catalysts (Fig. 4a and Fig. S8–S9).
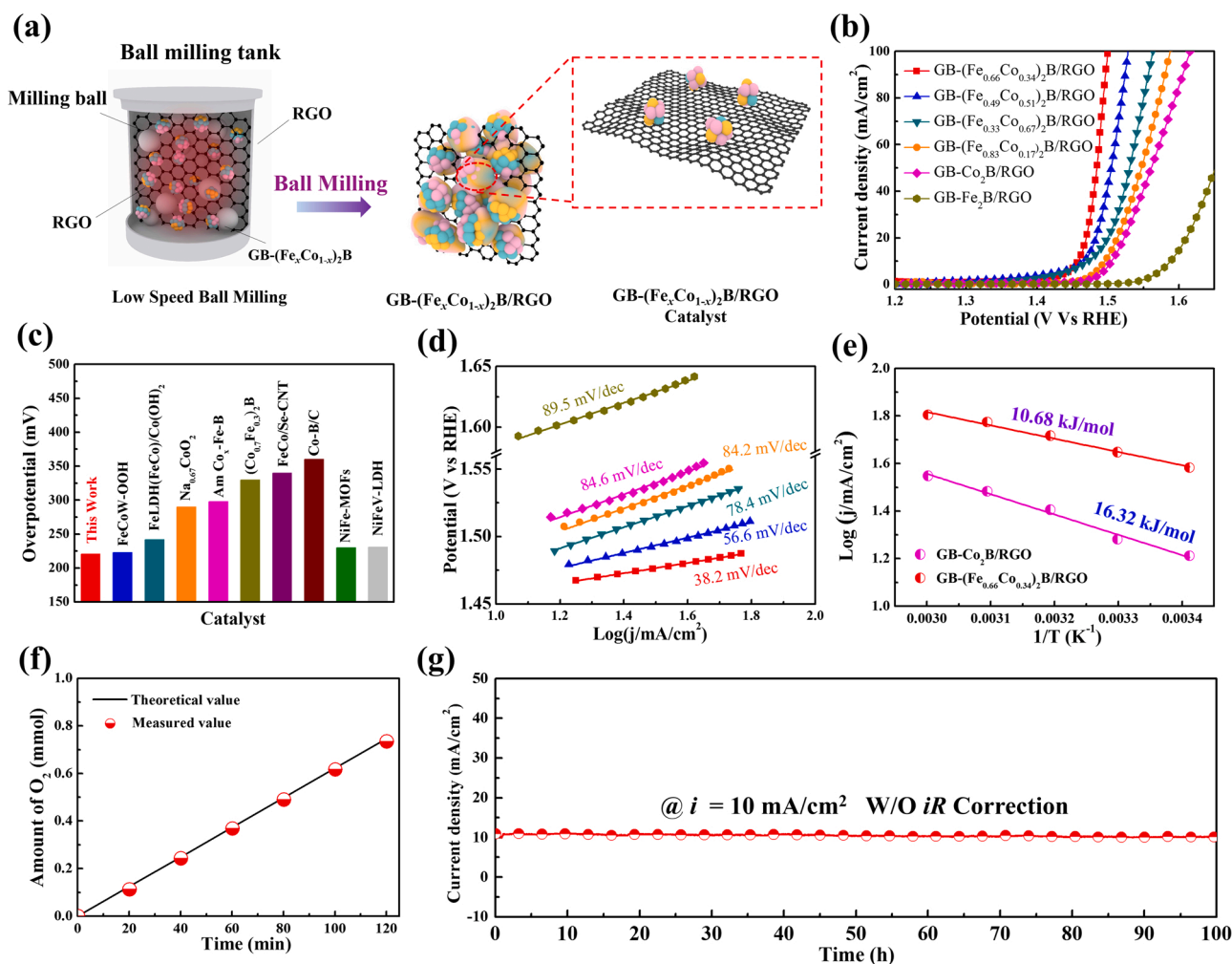

Fig. 3. OER performance of the as-prepared catalysts in 1.0 M KOH. (a) Synthesis process for GB-$(Fe_xCo_{1-x})_2B$/RGO catalyst. (b) LSV curves and (c) the corresponding over-potential comparison with current literature at 10 mA cm^{-2} and (d) Tafel plots. (e) The calculated reaction activation energy at 1.50 V. (f) The generated O_2 amount and (g) i-t curve of GB-$(Fe_{0.66}Co_{0.34})_2B$/RGO for 100 h at 1.46 V.

As shown in Fig. 4a, with the increase of Fe content, the C_{dl} values increase from 1.04 mF cm^{-2} (GB-Co$_2$B) to 2.16 mF cm^{-2} (GB-(Fe$_{0.33}$Co$_{0.67}$)$_2$B), reaching the maximum of 4.44 mF cm^{-2} for GB-(Fe$_{0.66}$Co$_{0.34}$)$_2$B. As the Fe amount further increases, the C_{dl} values sharply decrease to 1.34 mF cm^{-2} for GB-(Fe$_{0.83}$Co$_{0.17}$)$_2$B and 1.02 mF cm^{-2} for GB-Fe$_2$B. This result further demonstrates that the introduction of Fe into Co$_2$B can create more grain boundaries, which is a practical way to modulate the electrochemical surface area (ECSA) of GB-Co$_2$B. The increased ECSAs induced by more grain boundaries can boost the contact area between catalysts and electrolyte, which is conducive to improve the reaction kinetics and the charge transfer capacity at the electrode/electrolyte interface. Electrochemical impedance spectroscopy (EIS) measurements (Fig. 4b) is carried out to investigate the charge transfer behavior at the electrode/electrolyte interface, and an equivalent circuit model (the inset in Fig. 4b) is employed to estimate the solution resistance (R_s) and charge transfer resistance (R_{ct}). The fitting results reveal that GB-(Fe$_{0.66}$Co$_{0.34}$)$_2$B exhibits much lower R_s and R_{ct} values than other as-prepared catalysts, indicating this catalyst possesses the most favorable charge transfer kinetics for the OER process, which can be attributed to the fact that the increased grain boundary density favors the electron transmission at the electrode/electrolyte interface during OER processes [19]. In addition, the turnover frequency (TOF) values are also calculated to rule out the influences of grain boundaries density and ECSA on the catalytic activity, and the TOF values of GB-(Fe$_{0.66}$Co$_{0.34}$)$_2$B are significantly higher than

those of the other as-prepared catalysts (Fig. 4c), suggesting that the introduction of Fe in Co$_2$B can also increase the intrinsic activity. To further explain the modulation effect of Fe doping on the electronic structure of Co$_2$B, the DFT method is used to analyze changes in Co–B bond length, electron localization function, and density of states for GB-(Fe$_{0.66}$Co$_{0.34}$)$_2$ and GB-Co$_2$B catalysts (Fig. 4d–h). As shown in Figs. 4d and 4e, the GB-(Fe$_{0.66}$Co$_{0.34}$)$_2$ catalyst exhibits an increased Co–B bond length (2.158 Å) compared to pristine GB-Co$_2$B (2.125 Å), which is mainly because the introduction of Fe can weaken the interaction between Co and B. The electron localization functions in Figs. 4f and 4g show that the GB-(Fe$_{0.66}$Co$_{0.34}$)$_2$ catalyst exhibits a higher electron localization around B atoms compared to pristine GB-Co$_2$B, suggesting that the local electronic configuration of B can be regulated by introducing Fe atoms into GB-Co$_2$B. The non-bonding states B (B$_{NB}$) with specific local configurations might create boron holes, which accelerate the formation of MOO$^-$ species during OER processes [8]. The Total density of states (DOS) plot in Fig. 4h shows that the GB-(Fe$_{0.66}$Co$_{0.34}$)$_2$ catalyst exhibits an increased intensity near the Fermi level compared to GB-Co$_2$B, suggesting an enhanced electric conductivity, which accelerates the electron extraction process near the cobalt sites. The d-band centers of the Co atoms in GB-Co$_2$B and GB-(Fe$_{0.66}$Co$_{0.34}$)$_2$ are also calculated to investigate the electronic structures. Compared with Co$_2$B, the d-band center of GB-(Fe$_{0.66}$Co$_{0.34}$)$_2$ is upshifted toward the Fermi level (Fig. 4h), reducing the anti-bonding filling states in the d orbital and thus facilitating the adsorption of OER intermediates [45,46]. Based
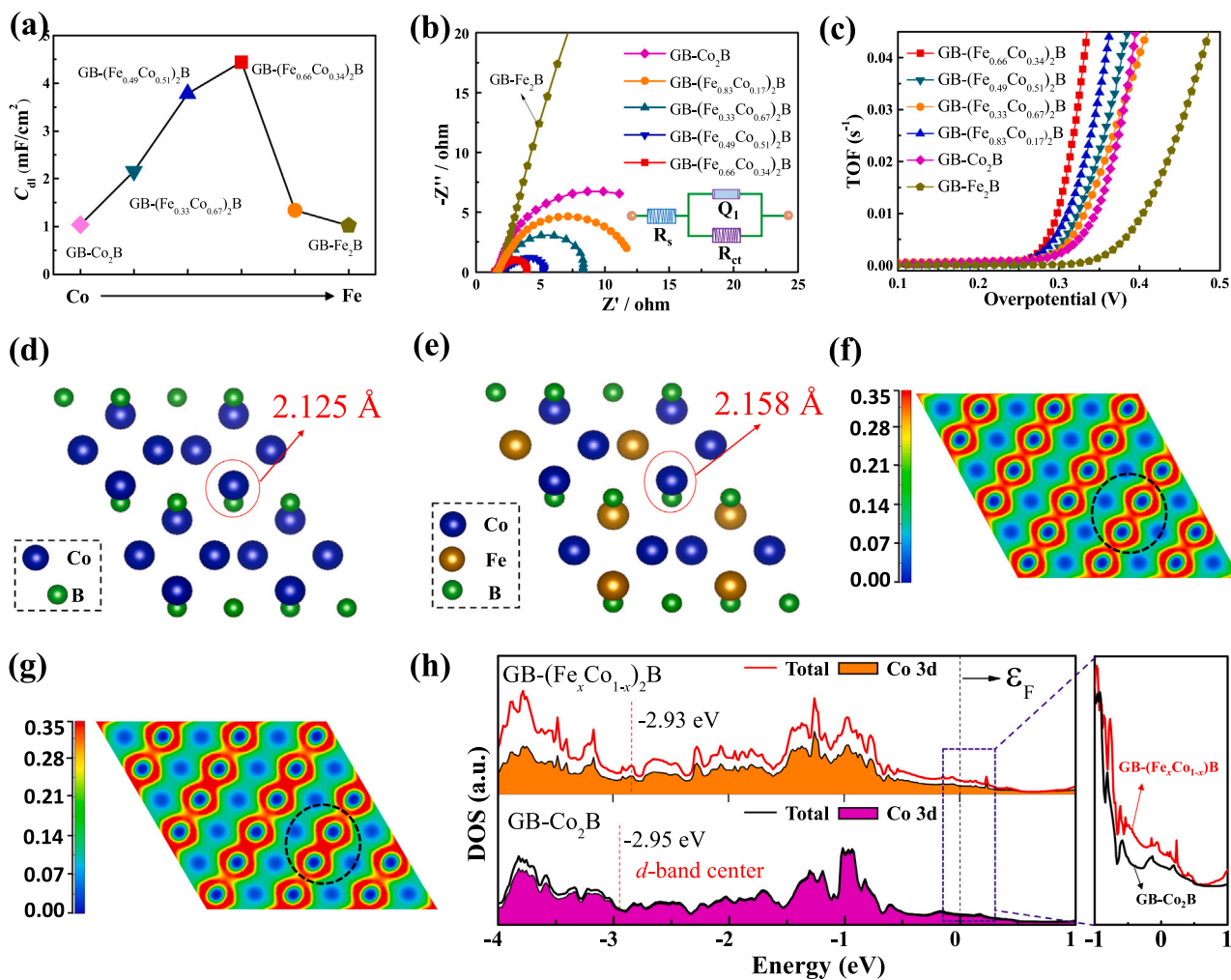

Fig. 4. (a) Influence of Co/Fe ratio on C_{dl} values. (b) Nyquist plots acquired at a potential of 1.531 V (versus the RHE) and corresponding equivalent circuit model, and (c) TOF values for GB-(Fe$_x$Co$_{1-x}$)$_2$B samples. (d,e) Optimized structural diagrams for pristine GB-Co$_2$B and GB-(Fe$_x$Co$_{1-x}$)$_2$B and corresponding two-dimensional electron localization function (f–g). (h) Co projected DOS, total DOS and calculated d-band center.

on these results, Fe doping can provide a higher grain boundary density and optimize the electronic structure of intermetallic Co_2B, favoring the electron transmission at the electrode/electrolyte interface and adsorption of OER intermediates during OER processes.

To examine the electro-catalytic behaviors, we conduct in-situ Raman measurement on GB-Co_2B and GB-$(Fe_{0.66}Co_{0.34})_2B$ in 1 M KOH (Fig. 5a and Fig. S10). The in-situ Raman spectra reveals a clear change with the increase of the applied potential. The growing intensity of characteristic peaks located at nearly 487 cm^{-1} and 581 cm^{-1} indicates that the formation of Co-OOH species on the electrode surface [47,48]. The two peak for GB-$(Fe_{0.66}Co_{0.34})_2B$ shows an obviously negative shift compared to GB-Co_2B at applied potentials of 0.3–0.6 V, indicating that the electronic configuration around Co sites and binding strength is changed due to the introduction of lattice strain in GB-Co_2B. [49]. Together with the results of the modulation for lattice strain by Fe doping (Figs. S3, 1e and 1i, 2a and 2c, 4d–f), it can be concluded that the lattice strain has a significant impact on the electronic configuration around metal sites [50–55], which could change the adsorption energy of the catalysts for OER intermediates and adjust the binding strength between catalyst surface and reaction intermediates [56,57]. Apparently, GB-$(Fe_{0.66}Co_{0.34})_2B$ exhibits a clear characteristic peak of MOO^- species at 1065 cm^{-1} when the applied potential is greater than 0.3 V (Fig. S11) [58,59], which is considered as active intermediates for OER, while the GB-Co_2B does not appear the peak until the applied potential is 0.6 V, confirming the faster formation kinetics of active intermediates. At any fixed applied potentials, the signal of Co-OOH in GB-$(Fe_{0.66}Co_{0.34})_2B$ is always higher than that of the Co_2B, further confirming the faster formation kinetics of active intermediates, which benefits from the modulation of both grain boundary density and electronic structure. Additionally, we have analyzed the changes of morphology and structure for GB-$(Fe_{0.66}Co_{0.34})_2B$ and after the OER 10 h using SEM, FTIR, XPS and XRD measurements. After the reaction for 10 h, SEM results (Fig. 5b) show that the surface of the particle-like shapes became rough at the grain boundaries, confirming that the grain boundaries are more favorable for the reaction [60]. This is mainly because the arrangement of atoms on the grain boundary is looser than that grain interior and there are many defects, such as vacancy, dislocation, and deformation. These defects can enhance the carrier transport along the defective conducting channels, which is beneficial to the water adsorption and activation on the catalyst surface [19,61,62]. The energy dispersive spectroscopy (EDS) elemental mapping and content results (Fig. 5b, Table S2) show an increased O content for the GB-$(Fe_{0.66}Co_{0.34})_2B$ sample after the OER, suggesting that GB-$(Fe_{0.66}Co_{0.34})_2B$ strongly favors the formation of intermediate species during the OER processes. Fig. 5c displays the several peaks at 1010–1200 cm^{-1}, which can be assigned to O_2^- species [20]. The intensity of O_2^- species can determine the O–O coupling ability, and the O–O bonding formation is considered as the rate-limiting step of OER [63,64]. The peak intensity in GB-$(Fe_xCo_{1-x})_2B$ increase first and then decrAppendix Aease with the increase of Fe content, indicating the O–O coupling ability can be controlled by changing the Fe content. Therefore, the GB-$(Fe_{0.66}Co_{0.34})_2B$ catalyst shows much higher OER activity. After OER, XPS O 2p

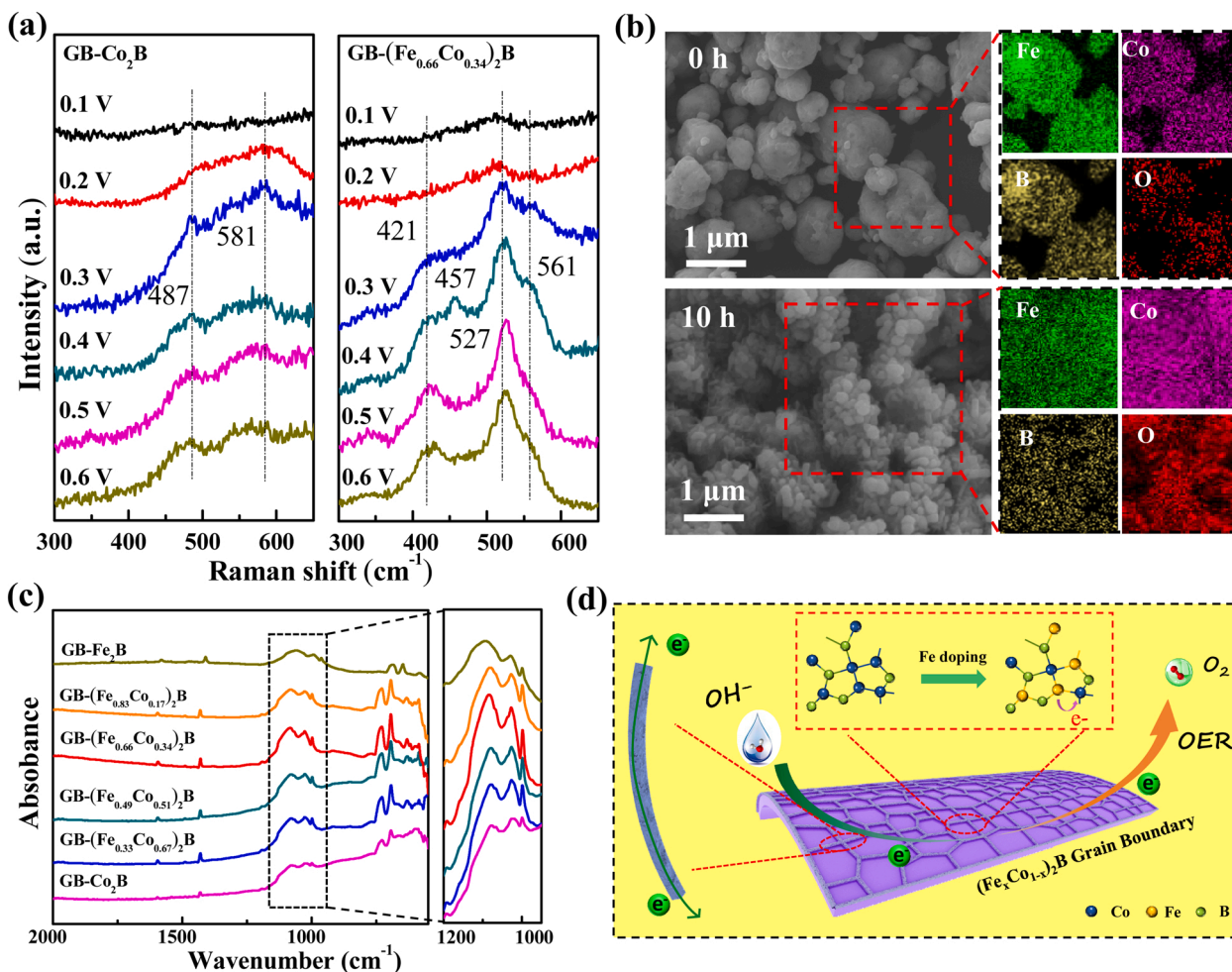**Fig. 5.** (a) In-situ Raman spectra collected on pristine GB-Co_2B and GB-$(Fe_{0.66}Co_{0.34})_2B$ under different applied potentials vs Ag/AgCl. (b) SEM images and corresponding EDS element mapping for the GB-$(Fe_{0.66}Co_{0.34})_2B$ and after the OER 10 h. (c) FTIR spectra. (d) OER activity enhancement mechanism schematic for GB-$(Fe_xCo_{1-x})_2B$ catalyst.

spectra (Fig. S11) shows an obvious increase in intensity of adsorbed O–O bonds (532.8 eV), further suggesting the formation of oxygenated intermediates species during the OER processes. Co 2p spectra show that the integral area of Co^{3+} is increased remarkably compared with the area of Co^{2+}, suggesting that the Co^{2+} species transform into Co^{3+} species (Co-OOH) during OER processes (Fig. S11c). XRD results plot in Fig. S12d reveal the peaks of GB-$(Fe_{0.66}Co_{0.34})_2B$ after OER 10 h are almost the same with GB-$(Fe_{0.66}Co_{0.34})_2B$ and no diffraction peaks of FeCo (oxy)hydroxide is observed, which can be explained by the low content and low crystallinity of in-situ formed the FeCo (oxy)hydroxide. Based on these results, the strong intensity of O_2^- species can be attributed to two important reasons (Fig. 5d): (i) the introduction of Fe in Co_2B can produce a higher density of grain boundaries, providing the more efficient actives sites and increase the probability of the intermediate formation. (ii) The electronic control effect of Fe doping can modify the local electronic structure and redox properties of the catalysts, promoting the formation of the OER intermediate products. Overall, all these results provide further evidence that the introduction of Fe into GB-Co_2B can create more grain boundaries density and optimize the electronic structure of intermetallic Co_2B, enhancing the OER activity of GB-$(Fe_{0.66}Co_{0.34})_2B$.

4. Conclusions

In summary, we used a simple ball milling approach to synthesize the intermetallic $(Fe_xCo_{1-x})_2B$ electro-catalysts with a high density of grain boundaries toward the oxygen evolution reaction in alkaline electrolytes. Benefiting from the modulation of both grain boundary density and electronic structure, the GB-$(Fe_{0.66}Co_{0.34})_2B$ supported on RGO exhibits an over-potential of 221 mV at the benchmark 10 mA cm^{-2} and a Tafel slope of 38.2 mV dec^{-1}. Meanwhile, we demonstrate that the introduction of Fe in intermetallic GB-Co_2B catalyst could produce a higher density of grain boundaries and modulate the electronic to accelerate the OER activity of GB-Co_2B. Furthermore, it is found that the higher grain boundaries density can provide the more efficient active site for the OER, due to the better electron transmission characteristics at the electrode/electrolyte interface. Moreover, the electronic control effect of Fe doping can modify the local electronic structure and redox properties of the catalysts, promoting the formation of the OER intermediate products during OER processes. This work provides a promising insights in the synergetic effects in bimetallic GB-$(Fe_xCo_{1-x})_2B$ systems and supports a new strategy to design highly efficient catalysts with a high density of grain boundaries using earth-abundant materials.

CRediT authorship contribution statement

Xianshu Qiao: Conceptualization, Methodology, Writing – original draft. **Hongjun Kang:** Assisted in the experiments, Writing-part of draft. **Yang Li:** Visualization, Revised the manuscript. **Kai Cui:** Density functional theory (DFT) calculations. **Xin Jia:** Data curation. **Xiaohong Wu:** Supervision, Supplied funding for the research. **Wei Qin:** Supervision, Supplied funding the research.

Associated Content

Supplemental Information

Additional SEM, EDS, and electrochemical characterization results. Tables for the calculated grain size of all samples and EDS element content results.

Declaration of Competing Interest

The authors declare that they have no known competing financial interests or personal relationships that could have appeared to influence the work reported in this paper.

Appendix A. Supporting information

Supplementary data associated with this article can be found in the online version at doi:10.1016/j.apcatb.2021.121034.

References

[1] J.J. Song, C. Wei, Z.F. Huang, C.T. Liu, L. Zeng, X. Wang, Z.C. Xu, A review on fundamentals for designing oxygen evolution electrocatalysts, Chem. Soc. Rev. 49 (2020) 2196–2214.

[2] H.Q. Zhou, F. Yu, J.Y. Sun, R. He, S. Chen, C.W. Chu, Z.F. Ren, Highly active catalyst derived from a 3D foam of Fe(PO$_3$)$_2$/Ni$_2$P for extremely efficient water oxidation, PNAS 114 (2017) 5607–5611.

[3] X. Fan, Q. Pang, S. Yi, X. Du, S. Zhang, Z. Liu, X. Yue, Intrinsic-structural-modulated carbon cloth as efficient electrocatalyst for water oxidation, Appl. Catal. B Environ. 292 (2021), 120152.

[4] S. Hao, Ya Wang, G. Zheng, L. Qiu, N. Xu, Y. He, L. Lei, X. Zhang, Tuning electronic correlations of ultra-small IrO$_2$ nanoparticles with La and Pt for enhanced oxygen evolution performance and long-durable stability in acidic media, Appl. Catal. B Environ. 266 (2020), 118643.

[5] K. Xu, P. Chen, X. Li, Y. Tong, H. Ding, X. Wu, W. Chu, Z. Peng, C. Wu, Y. Xie, Metallic nickel nitride nanosheets realizing enhanced electrochemical water oxidation, J. Am. Chem. Soc. 137 (2015) 4119–4125.

[6] J.M.V. Nsanzimana, Y.C. Peng, Y.Y. Xu, L. Thia, C. Wang, B.Y. Xia, X. Wang, An efficient and earth-abundant oxygen-evolving electrocatalyst based on amorphous metal borides, Adv. Energy Mater. 8 (2018) 1701475.

[7] L.C. Wang, J.X. Li, X.S. Zhao, W.J. Hao, X.H. Ma, S.J. Li, Y.H. Guo, Surface–activated amorphous iron borides (Fe$_x$B) as efficient electrocatalysts for oxygen evolution reaction, Adv. Mater. Interfaces 6 (2019), 1801690.

[8] W. Yuan, X. Zhao, W. Hao, Performance of surface–oxidized Ni$_3$B, Ni$_2$B and NiB$_2$ electrocatalysts for overall water splitting, ChemElectroChem 6 (2018) 764–770.

[9] Y.H. Guo, R.Q. Zhang, W.J. Hao, J.K. Zhang, Y.J. Yang, Multifunctional Co–B–O@ Co$_x$B catalysts for efficient hydrogen generation, Int. J. Hydrog. Energy 45 (2019) 380–390.

[10] J. Masa, D.P. Wei, D. Peeters, I. Sinev, W. Xia, Z.Y. Sun, C. Somsen, M. Muhler, W. Schuhmann, Amorphous cobalt boride (Co$_2$B) as a highly efficient nonprecious catalyst for electrochemical water splitting: oxygen and hydrogen evolution, Adv. Energy Mater. 6 (2016), 1502313.

[11] R. Kadrekara, N. Patelb, A. Arya, Understanding the role of boron and stoichiometric ratio in the catalytic performance of amorphous Co-B catalyst, Appl. Surf. Sci. 518 (2020), 146199.

[12] S. Anantharaj, S.R. Ede, K. Sakthikumar, K. Karthick, S. Mishra, S. Kundu, Recent trends and perspectives in electrochemical water splitting with an emphasis on sulfide selenide, and phosphide catalysts of Fe Co, and Ni: a review, ACS Catal. 6 (2016) 8069–8097.

[13] S.C. Tang, B.G. Zhu, X.L. Shi, J. Wu, X.K. Meng, General controlled sulfidation toward achieving novel nanosheet-built porous square-FeCo$_2$S$_4$-Tube arrays for high-Performance asymmetric all-solid-state pseudocapacitors, Adv. Energy Mater. 7 (2017), 1601985.

[14] B. Zhong, P. Kuang, L. Wang, J. Yu, Hierarchical porous nickel supported NiFeO$_x$H$_y$ nanosheets for efficient and robust oxygen evolution electrocatalyst under industrial condition, Appl. Catal. B Environ. 299 (2021), 120668.

[15] J.Z. Liu, Y.F. Ji, J.W. Nai, X.G. Niu, Y. Luo, L. Guo, S.H. Yang, Ultrathin amorphous cobalt–vanadium hydr(oxy)oxide catalysts for the oxygen evolution reaction, Energy Environ. Sci. 11 (2018) 1736–1741.

[16] H. Chu, D. Zhang, B. Jin, M. Yang, Impact of morphology on the oxygen evolution reaction of 3D hollow cobalt-molybdenum nitride, Appl. Catal. B Environ. 255 (2019), 117744.

[17] C.Y. Ling, Y.X. Ouyang, L. Shi, S.J. Yuan, Q. Chen, J.L. Wang, Template-grown MoS$_2$ nanowires catalyze the hydrogen evolution reaction: ultralow kinetic barriers with high active site density, ACS Catal. 7 (2017) 5097–5102.

[18] Z.Z. Sun, A. Curto, J. Rodríguez-Fernández, Z. Wang, A. Parikh, J. Fester, M. D. Dong, A. Vojvodic, J.V. Lauritsen, The Effect of Fe Dopant location in Co(Fe) OOH$_x$ nanoparticles for the oxygen evolution reaction, ACS Nano (2021), https://doi.org/10.1021/acsnano.1c07219.

[19] Y.M. He, P.Y. Tang, Z.L. Hu, Q.Y. He, Engineering grain boundaries at the 2D limit for the hydrogen evolution reaction, Nat. Commun. 11 (2019) 57.

[20] W.R. Cheng, X. Zhao, H. Su, F.M. Tang, W. Che, H. Zhang, Q.H. Liu, Lattice-strained metal–rganic-framework arrays for bifunctional oxygen electrocatalysis, Nat. Energy 4 (2019) 115–122.

[21] D.J. Zhou, S.Y. Wang, Y. Jia, X.Y. Xiong, H.B. Yang, S. Liu, J.L. Tang, J.M. Zhang, D. Liu, L.R. Zheng, Y. Kuang, X.M. Sun, B. Liu, NiFe hydroxide lattice tensile strain: enhancement of adsorption of oxygenated intermediates for efficient water oxidation catalysis, Angew. Chem. Int. Ed. 58 (2019) 736–740.

[22] Z. Hegedus, S. Meka, E. Mittemeijer, In situ consolidation of ball milled metals, J. Alloy. Comp. 695 (2017) 721–725.

[23] N.H. Heo, K.H. Chai, J.G. Na, Correlation between interfacial segregation and surface-energy-induced selective grain growth in 3% silicon–iron alloy, Acta Mater. 48 (2000) 2901–2910.

[24] Y. Gao, Y. Zhang, B.W. Beeler, Y. Wang, Self-organized multigrain patterning with special grain boundaries produced by phase transformation cycling, Phys. Rev. Mater. 2 (2018), 073402.

[25] Y. Liang, Z. Wu, E. Fu, J. Du, P. Wang, Y. Zhao, Y. Qiu, Z. Hu, Refinement process and mechanisms of tungsten powder by high energy ball milling, Int. J. Refract. Met. H. 67 (2017) 1–8.

[26] Z. Huang, L. Chen, B. Huang, B. Xu, G. Shao, H. Wang, Y. Li, C. Wang, Enhanced performance of Li$_{6.4}$La$_3$Zr$_{1.4}$Ta$_{0.6}$O$_{12}$ solid electrolyte by the regulation of grain and grain boundary phases, ACS Appl. Mater. Interfaces 12 (2020) 56118–56125.

[27] Y. Zhu, Z. Xu, Q. Lang, W. Jiang, Q. Yin, S. Zhong, S. Bai, Grain boundary engineered metal nanowire cocatalysts for enhanced photocatalytic reduction of carbon dioxide, Appl. Catal. B Environ. 206 (2017) 282–292.

[28] H. Park, H. Ahn, T. Lee, J. Lee, M. Gyoung Lee, S.A. Lee, J. Yang, S. Kim, S. Ahn, S. Kim, C. Lee, E. Park, H. Jang, Grain boundaries boost oxygen evolution reaction in NiFe electrocatalysts, Small Methods 5 (2021) 2000755.

[29] L. Sun, Z. Dai, L. Zhong, Y. Zhao, Y. Cheng, S. Chong, G. Chen, C. Yan, X. Zhang, H. Tan, L. Zhang, K.N. Dinh, S. Li, F. Ma, Q. Yan, Lattice strain and atomic replacement of CoO$_6$ octahedra in layered sodium cobalt oxide for boosted water oxidation electrocatalysis, Appl. Catal. B Environ. 297 (2021) 120477.

[30] X.Q. Lu, M.Z. Ao, X.X. Tian, W.Y. Zan, Y.M. Mu, S.D. Li, Perfect cubic La-doped boron clusters La$_6$-[La@B$_{24}$] +/0 as the embryos of low-dimensional lanthanide boride nanomaterials, RSC Adv. 10 (2020) 12469–12474.

[31] Y.J. Qu, M.M. Shao, Y.F. Shao, M.Y. Yang, J.C. Xu, C.T. Kwok, X.Q. Shi, Z.G. Lu, H. Pan, Ultra-high electrocatalytic activity of VS$_2$ nanoflowers for efficient hydrogen evolution reaction, J. Mater. Chem. A 5 (2017) 1580–1586.

[32] M. Biesinger, B. Payne, A. Grosvenor, L. Lau, A. Gerson, R. Smart, Resolving surface chemical states in XPS analysis of first row transition metals, oxides and hydroxides: Cr, Mn, Fe, Co and Ni, Appl. Surf. Sci. 257 (2011) 2717–2730.

[33] Y. Wang, Y. Zhang, Z. Liu, C. Xie, S. Feng, D. Liu, M. Shao, S. Wang, Layered double hydroxide nanosheets with multiple vacancies obtained by dry exfoliation as highly efficient oxygen evolution electrocatalysts, Angew. Chem. Int. Ed. 56 (2017) 5867–5871.

[34] C. Roy, B. Sebok, S. Scott, E. Fiordaliso, J. Sørensen, A. Bodin, D. Trimarco, C. Damsgaard, P. Vesborg, O. Hansen, I. Stephens, J. Kibsgaard, I. Chorkendorff, Impact of nanoparticle size and lattice oxygen on water oxidation on NiFeO$_x$H$_y$, Nat. Catal. 1 (2018) 820–829.

[35] B. Zhang, X. Zheng, O. Voznyy, R. Comin, M. Bajdich, M. Garcia-Melchor, J. Han, M. Xu, L. Liu, F. Zheng, C. Garciade Arquer, F. Dinh, M. Fan, E. Yuan, N. Yassitepe, T. Chen, P. Regier, Y. Liu, P. Li, A. De Luna, H. Janmohamed, H. Xin, A. Yang, E. Vojvodic, Homogeneously dispersed multimetal oxygen-evolving catalysts, Science 352 (2016) 333–337.

[36] F. Kong, W. Zhang, L. Sun, H. Huo, Interface electronic coupling in hierarchical FeLDH(FeCo)/Co(OH)$_2$ arrays for efficient electrocatalytic oxygen evolution, ChemSusChem 12 (2019) 3592–3601.

[37] H. Wang, J. Wu, A. Dolocana, Y. Li, X. Lü, N. Wu, K. Park, S. Xin, M. Lei, W. Yang, J. Goodenough, Short O–O separation in layered oxide Na$_{0.67}$CoO$_2$ enables an ultrafast oxygen evolution reaction, P Natl. Acad. Sci. Usa. 116 (2019) 23473–23479.

[38] H. Chen, S. Ouyang, M. Zhao, Y. Li, Synergistic activity of Co and Fe in amorphous Co$_x$–Fe–B catalyst for efficient oxygen evolution reaction, ACS Appl. Mater. Interfaces 9 (2017) 40333–40343.

[39] S. Klemenz, J. Schuch, S. Hawel, A. Zieschang, B. Kaiser, W. Jaegermann, B. Albert, Synthesis of a highly efficient oxygen-evolution electrocatalyst by incorporation of iron into nanoscale cobalt borides, ChemSusChem 11 (2018) 3150–3156.

[40] H. Zhang, M. Zhao, H. Liu, S. Shi, Z. Wang, B. Zhang, L. Song, J. Shang, Y. Yang, C. Ma, L. Zheng, Y. Han, W. Huang, Ultrastable FeCo bi-functional electrocatalyst on Se-doped CNTs for liquid and flexible all-solid-state rechargeable Zn–Air batteries, Nano Lett. 21 (2021) 2255–2264.

[41] Y. Li, H. Xu, H. Huang, L. Gao, Y. Zhao, T. Ma, Synthesis of Co-B in porous carbon using a metal–organic framework (MOF) precursor: A highly efficient catalyst for the oxygen evolution reaction, Electrochem. Commun. 86 (2018) 140–144.

[42] Q. Ji, Y. Kong, C. Wang, H. Tan, H. Duan, W. Hu, G. Li, Y. Lu, N. Li, Y. Wang, J. Tian, Z. Qi, Z. Sun, F. Hu, W. Yan, Lattice strain induced by linker scission in Metal–Organic framework nanosheets for oxygen evolution reaction, ACS Catal. 10 (2020) 5691–5697.

[43] K. Ngoc Dinh, P. Zheng, Z. Dai, Y. Zhang, R. Dangol, Y. Zheng, B. Li, Y. Zong, Q. Yan, Ultrathin porous NiFeV ternary layer hydroxide nanosheets as a highly efficient bi-functional electrocatalyst for overall water splitting, Small 14 (2018) 1703257.

[44] J. Liu, Q. Hu, Y. Wang, Z. Yang, X. Fan, L. Liu, L. Guo, Achieving delafossite analog by in situ electrochemical self-reconstruction as an oxygen-evolving catalyst, P Natl. Acad. Sci. Usa. 36 (2020) 21906–21913.

[45] J. Kitchin, J. Nørskov, M. Barteau, Role of strain and ligand effects in the modification of the electronic and chemical Properties of bimetallic surfaces, J. Chem, Phys. Rev. Lett. 93 (2004), 156801.

[46] F. Cheng, J. Shen, B. Peng, Y. Pan, Z. Tao, J. Chen, Rapid room-temperature synthesis of nanocrystalline spinels as oxygen reduction and evolution electrocatalysts, Nat. Chem. 3 (2011) 79–84.

[47] Z. Chen, L. Cai, X. Yang, C. Kronawitter, L. Guo, S. Shen, B. Koel, Reversible structural evolution of NiCoO$_x$H$_y$ during the oxygen evolution reaction and identification of the catalytically active phase, ACS Catal. 8 (2018) 1238–1247.

[48] Z. Kou, Y. Yu, X. Liu, X. Gao, L. Zheng, H. Zou, Y. Pang, Z. Wang, Z. Pan, J. He, S. Pennycook, J. Wang, Potential-dependent phase transition and Mo-enriched surface reconstruction of γ-CoOOH in a hetero-structured Co-Mo$_2$C Pre-catalyst enable water oxidation, ACS Catal. 10 (2020) 4411–4419.

[49] Y. Wang, X. Li, M. Zhang, Y. Zhou, D. Rao, C. Zhong, J. Zhang, X. Han, W. Hu, Y. Zhang, K. Zaghib, Y. Wang, Y. Deng, Lattice-strain engineering of a homogeneous NiS$_{0.5}$Se$_{0.5}$ core–shell nanostructure as a highly efficient and robust electrocatalyst for overall water splitting, Adv. Mater. 32 (2020), 2000231.

[50] X.C. Du, J.W. Huang, J.J. Zhang, Y.C. Yan, C.Y. Wu, Y. Hu, C.Y. Yan, T.Y. Lei, W. Chen, C. Fan, J. Xiong, Modulating electronic structures of inorganic nanomaterials for efficient electrocatalytic water splitting, Angew. Chem. Int. Ed. 58 (2019) 4484–4502.

[51] Q.C. Feng, S. Zhao, D.S. He, S.B. Tian, L. Gu, X.D. Wen, C. Chen, Q. Peng, D. S. Wang, Y.D. Li, Strain engineering to enhance the electro-oxidation performance of atomic-Layer Pt on intermetallic Pt$_3$Ga, J. Am. Chem. Soc. 140 (2018) 2773–2776.

[52] P. Strasser, S. Koh, T. Anniyev, J. Greeley, K. More, C. Yu, Z. Liu, S. Kaya, D. Nordlund, H. Ogasawara, M.F. Toney, A. Nilsson, Lattice-strain control of the activity in de-alloyed core–shell fuel cell catalysts, Nat. Chem. 2 (2010) 454–460.

[53] D. Voiry, H. Yamaguchi, J. Li, R. Silva, D. Alves, T. Fujita, M. Chen, T. Asefa, V. Shenoy, G. Eda, M. Chhowalla, Enhanced catalytic activity in strained chemically exfoliated WS$_2$ nanosheets for hydrogen evolution, Nat. Mater. 12 (2013) 850–855.

[54] A. Sengeni, K. Subrata, N. Suguru, "The Fe Effect": A review unveiling the critical roles of Fe in enhancing OER activity of Ni and Co based catalysts, Nano Energy 80 (2021), 105514.

[55] X. Qiao, H. Kang, J. Wu, Y. Li, Q. Wang, X. Jia, Y. Qiao, S. Lu, X. Wu, W. Qin, A partial sulfidation approach that significantly enhance the activity of FeCo layered double hydroxide for oxygen evolution reaction, Int. J. Hydrog. Energ. 60 (2019) 31987–31994.

[56] S. Schnur, A. Gross, Strain and coordination effects in the adsorption properties of early transition metals: A density-functional theory study, Phys. Rev. B 81 (2010), 033402.

[57] D. Wang, H. Xin, R. Hovden, H. Wang, Y. Yu, D.A. Muller, F.J. DiSalvo, H. D. Abruna, Structurally ordered intermetallic platinum–cobalt core–shell nanoparticles with enhanced activity and stability as oxygen reduction electrocatalysts, Nat. Mater. 12 (2013) 81–87.

[58] B. Trzesniewski, O. Diaz-Morales, D. Vermaas, A. Longo, W. Bras, M. Koper, W. Smith, In situ observation of active oxygen species in Fe-containing Ni-based oxygen evolution catalysts: The effect of pH on electrochemical activity, J. Am. Chem. Soc.. 137 (2015) 15112–15121.

[59] X. Ma, K. Zhao, Y. Sun, Y. Wang, F. Yan, X. Zhang, Y. Chen, Direct observation of chemical origins in crystalline (Ni$_x$Co$_{1-x}$)$_2$B oxygen evolution electro-catalysts, Catal. Sci. Technol. 10 (2020) 2165–2172.

[60] Y. Heo, S. Choi, J. Bak, H. Kim, H. Bae, S. Chung, Symmetry-broken atom configurations at grain boundaries and oxygen evolution electrocatalysis in perovskite oxides, Adv. Energy Mater. 8 (2018), 1802481.

[61] B. Kumar, V. Atla, J.P. Brian, S. Kumari, T.Q. Nguyen, M. Sunkara, J.M. Spurgeon, Reduced SnO$_2$ porous nanowires with a high Density of grain boundaries as catalysts for efficient electrochemical CO$_2$-into-HCOOH conversion, Angew. Chem. Int. Ed. 56 (2017) 3645–3649.

[62] R.R. Zhang, Y.C. Zhang, L. Pan, G.Q. Shen, N. Mahmood, Y.H. Ma, Y. Shi, W.Y. Jia, L. Wang, X.W. Zhang, W. Xu, J.J. Zou, Engineering cobalt defects in cobalt oxide for highly efficient electrocatalytic oxygen evolution, ACS Catal. 8 (2018) 3803–3811.

[63] G. Zhao, P. Li, N. Cheng, S. Dou, W. Sun, An Ir/Ni(OH)$_2$ heterostructured electrocatalyst for the oxygen evolution reaction: breaking the scaling relation, stabilizing iridium(V), and beyond, Adv. Mater. 32 (2020), 2000872.

[64] K. Jiang, M. Luo, M. Peng, Y. Yu, Y. Lu, T. Chan, P. Liu, F. Groot, Y. Tan, Dynamic active-site generation of atomic iridium stabilized on nanoporous metal phosphides for water oxidation, Nat. Commun. 11 (2020) 2701.